



# Janus MoWC MXene for Efficient Nitrogen Reduction: A DFT Study

Anju Rajan<sup>1</sup> and Raghu Chatanathodi<sup>1,\*</sup>

<sup>1</sup> Department of Physics, National Institute of Technology Calicut, Kerala, India

\* [raghuc@nitc.ac.in](mailto:raghuc@nitc.ac.in)

**Abstract.** In this study, we report the design and investigation of a Janus MoWC monolayer, derived from pristine Mo<sub>2</sub>C MXene through first-principles calculations based on density functional theory (DFT). By introducing compositional asymmetry in the MXene structure, we aim to tune its electronic and catalytic properties for enhanced nitrogen reduction reaction (NRR) performance. The thermal and dynamical stabilities of the Janus MoWC monolayer are systematically evaluated, confirming that the material is both stable and viable for catalytic applications. Our calculations reveal that the asymmetric structure significantly strengthens the adsorption of N<sub>2</sub> molecules compared to its pristine counterpart, thereby facilitating the activation of the inert N≡N bond. The analysis of the NRR pathways shows that the Janus MoWC monolayer prefers an enzymatic mechanism, with a free energy change of only 0.52 eV for the rate determining step. The enhanced N<sub>2</sub> adsorption capacity, coupled with favorable energetics and robust structural stability, suggests that the Janus MoWC monolayer could serve as an effective catalyst for sustainable ammonia production.

**Keywords:** Density Functional Theory, MXenes, Nitrogen Reduction Reaction.

## 1 Introduction

Ammonia (NH<sub>3</sub>) plays a crucial role in a wide range of applications, from enhancing agricultural productivity to serving as a key industrial chemical [1]- [3]. Its economic and environmental significance has driven the search for highly active and selective catalysts for the nitrogen reduction reaction (NRR) [4]. However, current industrial ammonia production methods, mainly the Haber–Bosch process face inherent limitations, as they require harsh conditions like high temperatures (350-550 °C) and pressures (150-350 atm), leading to substantial energy consumption [2], [5], [6]. This challenge comes from the strong triple bond (N≡N) and high bond dissociation energy in molecular nitrogen, which is difficult to cleave under ambient conditions. Moreover, the similar reduction potentials of nitrogen and the hydrogen evolution reaction (HER) hinder effective N<sub>2</sub> adsorption and activation on electrode surfaces [7]. To overcome these barriers, the development of highly efficient electro catalysts with superior selectivity is essential, aiming to lower the NRR energy threshold while suppressing the

competing HER. To date, a number of metal-based materials have been widely investigated as NRR catalysts. The availability of d-orbital electrons which can facilitate the  $\pi$ -back donation process makes transition metal based materials prominent. However, their practical application is often limited by high cost, scarcity, poor selectivity, or limited durability. As a result, the development of novel, efficient electro catalysts for NRR remains a significant challenge in the field.

Recent advances in low-dimensional materials, especially those containing transition metals have unveiled structures with remarkable properties, arising from their variable oxidation states and strong spin-orbit coupling. These distinctive features make them highly attractive for both fundamental studies and practical applications. Among these materials, MXenes stand out as a prominent class of two-dimensional (2D) transition metal carbides and nitrides, typically expressed by the formula  $M_{n+1}X_n$ , where M is a transition metal, X is carbon or nitrogen, and n ranges from 1 to 3 [8]– [10]. Experimentally, MXene can be prepared from their MAX phase by the chemical exfoliation of Al under wet HF conditions, resulting in the 2D form [11], [12]. MXenes are attractive due to their outstanding chemical and mechanical stability, structural tunability across monolayer to multilayer forms, and the flexibility to incorporate a wide range of transition metals.

The pioneering Janus monolayer structure was first reported by Lu et al., representing a major breakthrough in materials science. They successfully synthesized MoSSe by modifying the conventional MoS<sub>2</sub> structure, introducing out-of-plane asymmetry that significantly enhanced the Rashba effect [13]. Subsequent theoretical studies were done to investigate the catalytic activities of Janus TMDs. Most of the Janus TMDs were found to be catalytically very active towards HER [14], [15]. Similarly, MXenes also can be altered into their corresponding Janus structures. In M<sub>2</sub>X kind of MXenes C or N atoms are sandwiched between the transition metal layers. One of the metal layers can be replaced with another transition metal layer which can lead to the formation of MM'X type Janus structures. Akgen et.al explored the electronic, magnetic, and structural properties of Cr based MM'C Janus structures. These materials were found to show unique electronic and magnetic properties [16]. Madira et.al explored the potential of some MM'C kind MXenes towards electrodes in super capacitors, highlighting that the charge storage capacity is enhanced by the surface engineering process [17]. 2H phase of Janus MoWC MXene is identified as the most stable configuration, showing superior mechanical strength due to strong C–C bonding and withstanding up to 9% tensile strain. Additionally, 2H-MoWC is identified as a superconductor with a T<sub>c</sub> of 1.6 K, which increases to 7 K under biaxial strain, making it a promising material for 2D straintronic applications [18].

Inspired from the exceptional characteristics of Janus MXene structures, this study explores the NRR activity of MoWC MXene using Density Functional Theory (DFT). The Janus structure is engineered from the corresponding parent material Mo<sub>2</sub>C. The NRR activity is primarily investigated from the N<sub>2</sub> adsorption strength and N<sub>2</sub> activation. To validate the catalytic activity, the theoretical over potential is calculated from the free energy diagram and limiting potential. In addition, a selectivity analysis is conducted to assess the ability of the material to suppress the competing HER [19].

## 2 Computational methods and models

DFT computations are carried out using Vienna ab initio Simulation Package (VASP) [20] [21]. The exchange correlation part is treated by the Perdew–Burke–Ernzerhof (PBE)[22] functional in the frame work of Generalized Gradient Approximation (GGA). Projector Augmented Wave (PAW)[23] pseudopotential is used to approximate the core-valence interactions. Long range Vander waals interactions are accounted by empirical correction in Grimme’s method (DFT + D2) [24] as implemented in VASP. Geometry optimizations are performed with an energy convergence of  $10^{-4}$  and a force convergence of  $10^{-3}$  eVÅ<sup>-1</sup>. An energy cutoff of 460 eV is utilized in the expansion of the plane wave basis sets for the optimization of the monomer unit cell. K-point sampling of  $17 \times 17 \times 17$  and  $5 \times 5 \times 1$  are used for the monomer unit cell and supercell respectively employing the Monkhorst-Pack[25]. A  $4 \times 4$  supercell is used to study HER activity. A 20 Å vacuum is added along the z-direction to avoid any unphysical interaction between periodic images. To evaluate the catalytic potential, Gibbs free energy ( $\Delta G$ ) is evaluated for all the elementary steps in the NRR process employing the Computational Electrode Model (CHE)[19], [26]. The  $\Delta G$  is calculated using the equation,

$$\Delta G = \Delta E + \Delta ZPE - T\Delta S + \Delta G_{pH} \quad (1)$$

Where  $\Delta E$  is the difference in total energy obtained from VASP calculations,  $\Delta ZPE$  term denotes the zero-point energy difference, obtained by calculating the vibrational frequencies of the corresponding species, and  $\Delta S$  represents the entropy change evaluated at room temperature ( $T = 298.15$  K).  $\Delta G_{pH}$  is the free energy contribution due to proton concentration, obtained using the equation  $\Delta G_{pH} = 2.303k_B T \text{ pH}$  and pH is set to 0, corresponding to strongly acidic conditions. The free energy diagram is plotted based on the calculated  $\Delta G$  values of elementary steps and the limiting potential is calculated as,

$$U_L = -\max(\Delta G_1, \Delta G_2, \Delta G_3 \dots \Delta G_n)/e \quad (2)$$

to evaluate the NRR activity.

The adsorption energy for different adsorbates is calculated using the equation,

$$E_{ads} = E_{total} - (E_{mono} + E_{mol}) \quad (3)$$

Here  $E_{total}$  is the total energy after adsorption,  $E_{mono}$  represents the energy of the monolayer and  $E_{mol}$  is the energy of the adsorbate.

## 3 Results and Discussions

### 3.1 Geometrical structure and electronic properties

For constructing Janus MoWC, initially we have optimized the structure of the parent material Mo<sub>2</sub>C. 2D Mo<sub>2</sub>C can be derived by selectively removing the Al layer from its

$\text{Mo}_2\text{AlC}$  MAX phase. In  $\text{Mo}_2\text{C}$ , carbon layer is sandwiched between two layers of Mo atoms, forming hexagonal lattice classified under the space group  $P6m2$ . The optimized lattice parameters of the unit cell are  $a=b=2.87\text{\AA}$  which is well agreeing with the previous results [27] and the Mo-C bond length is calculated to be  $2.12\text{\AA}$ . The 2D Janus MXene is obtained from  $\text{Mo}_2\text{C}$  by replacing one of the Mo layer by W layer thereby breaking the structural symmetry as shown in Figure 1a. The optimized Janus structure exhibits a lattice parameter of  $2.82\text{\AA}$ . The Mo-C bond length is slightly reduced to  $2.10\text{\AA}$  and W-C bond length is increased to  $2.15\text{\AA}$  which indicates the symmetry disruption due to Janus functionalization.

The dynamical stability of both structures are confirmed from the phonon dispersion along the high symmetry points of the Brillouin zone  $\Gamma\text{-M-K-}\Gamma$  as shown in figure 1b. The phonon dispersion reveals nine phonon modes, with no imaginary frequencies observed. Ab-initio Molecular Dynamics (AIMD) simulations were conducted to evaluate the thermal stability of the structure at elevated temperatures. The simulations were performed in a canonical (NVT) ensemble at 300 K using the Nose–Hoover thermostat for temperature regulation, with a time step of 1.0 fs over 5000 steps, as illustrated in figure 1c. Both materials are found to retain their structure after simulation, indicating structural stability at room temperature.

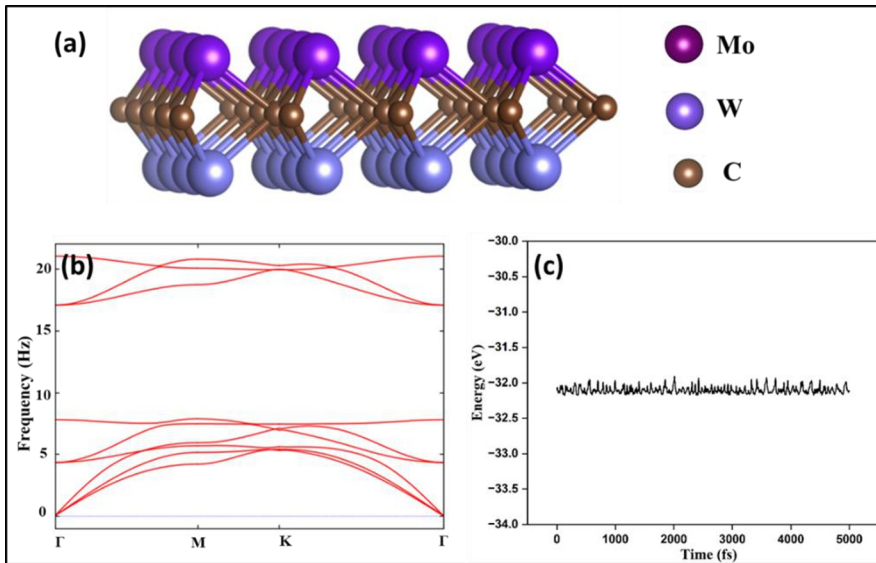


**Fig. 1.** (a) Optimized supercell of MoWC (b) Phonon dispersion and (c) AIMD simulation of MoWC.

Electronic structure of Janus MoWC is analyzed from Density of States (DOS) and band dispersion. The material is found to be non-magnetic in nature. From the projected density of states (PDOS) and band dispersion in figure 2, it is clear that multiple bands

are crossing the fermi level indicating the metallic behavior. Hence Janus structure retains the metallic character and conductivity of the parent material. PDOS indicates that main contribution near the fermi level comes from the Mo and W d-orbitals.

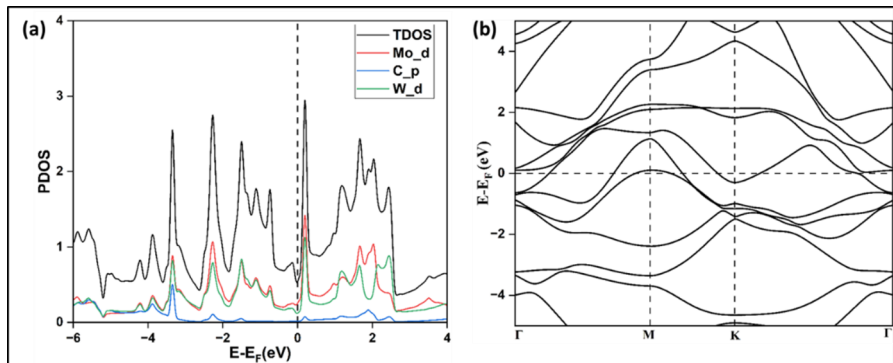


**Fig. 2.** (a) PDOS and (b) band dispersion of MoWC MXene.

### 3.2 N<sub>2</sub> adsorption and activation

A strong N<sub>2</sub> adsorption and activation are the pre requisites for NRR. In order to investigate N<sub>2</sub> adsorption on Janus MoWC, a 4×4 supercell is modeled. N<sub>2</sub> adsorption can be carried out on three possible sites T1, H1 and H2 as shown in figure 3a. Also, two possible adsorption configurations of N<sub>2</sub> molecule are studied; side-on and end on configurations (Figure 3b and 3c). The calculated adsorption energy values and N≡N bond lengths are tabulated in table1. A more negative value of adsorption energy indicates stronger binding between N<sub>2</sub> and the 2D MXene surface, indicating enhanced activation of the nitrogen molecule. The calculated adsorption energies indicate that maximum adsorption and bond stretching is occurring on H2 site with side on configuration. Here two N atoms are interacting with the three adjacent metal atoms. Hence further analysis is based on this configuration.

**Table.1.** N<sub>2</sub> adsorption energy and bond lengths at different sites.

Site	E <sub>ads</sub> (eV)	Bond length (Å)
T1-end on	-0.93	1.13
T1-side on	-0.16	1.14
H1-end on	-0.18	1.18
H1-side on	-1.52 (shift to H2)	1.33
H2-end on	-0.94	1.14
H2-side on	-1.52	1.33

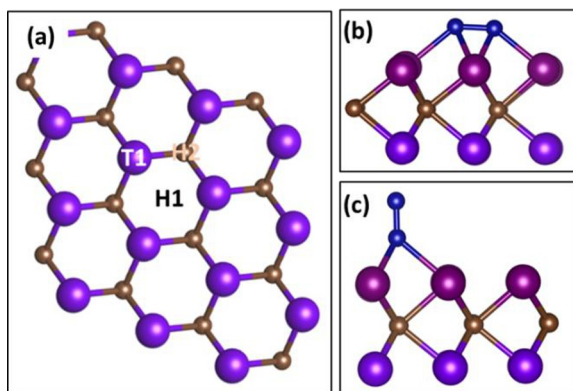


**Fig. 3.** (a) Possible adsorption sites on MoWC (b) side-on configuration and (c) End-on configuration

The amount charge transfers between the catalyst and N<sub>2</sub> molecule is studied using Bader charge analysis [28]. A net charge of 1.27e is transferred from the catalyst to the molecule. For better understanding, the Charge Density Difference (CDD) is plotted in Figure 4b. There is a notable charge depletion between the N≡N bond which indicates the weakening of the strong triple bond. A charge accumulation which is an indicative of bonding is also observed between the N atoms and bonded metals. The electron donation and back donation mechanism is visible from the CDD plot. Mo has empty d orbitals to accept lone pair of electrons from N<sub>2</sub> molecule, simultaneously Mo can donate d electrons back to the anti-bonding  $\pi^*$  orbital of N<sub>2</sub>. It implies that N<sub>2</sub> can act as both electron donor and acceptor at the same time. The charge depletion around the bond and accumulation near the N atoms validates the mechanism.

For more insights, PDOS of the adsorbed configuration is analyzed, which is shown in figure 4a. Significant hybridization is observed between the metal d orbital and the N<sub>2</sub> molecule. On adsorption, the N<sub>2</sub>  $\pi^*$  orbital interacts with Mo-d orbital to form the partially occupied d- $\pi^*$  orbitals. While, Mo-d orbital and N<sub>2</sub>  $\sigma$  orbital hybridize to form the occupied d- $\sigma$  orbitals. It provides evidence for the back donation mechanism.

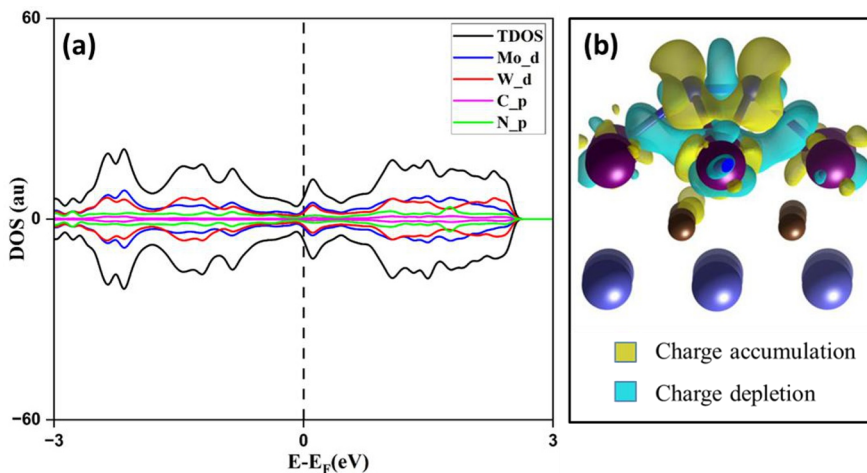
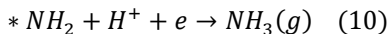
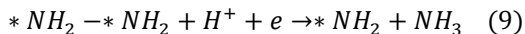
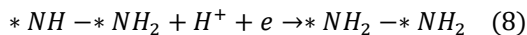
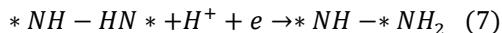
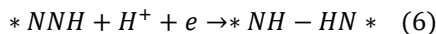
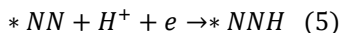
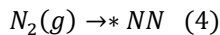


Fig. 4. (a) PDOS and (b) Charge density difference plot for  $N_2$  adsorbed system.

### 3.3 The reduction mechanism and selectivity

NRR can proceed through six coupled proton and electron transfer steps which can be represented as,



The NRR can follow either alternating, distal or enzymatic mechanisms. End-on configurations generally follow alternating or distal mechanisms and side-on configuration follow enzymatic mechanism. All these mechanisms involve the transfer of six protons and six electrons, and yielding two molecules of  $NH_3$ . In the distal pathway, the proton-electron pairs ( $H^+ + e^-$ ) initially attack the nitrogen atom farther from the MXene surface active site to produce the first  $NH_3$  molecule, followed by protonation of the second nitrogen to generate the second  $NH_3$ . In contrast, the alternating and enzymatic

pathways involve sequential protonation of both adsorbed nitrogen atoms as shown in Figure 5. Since the most stable adsorbed configuration for MoWC is side-on, we are investigating the enzymatic mechanism only.

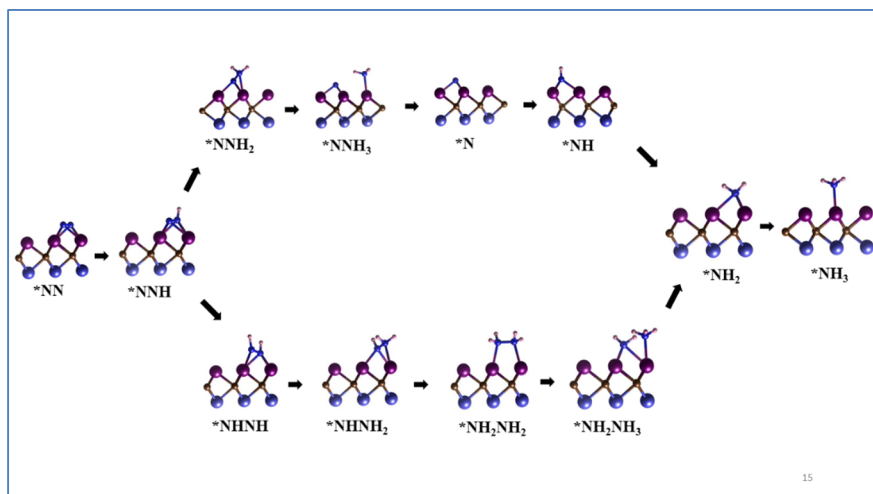


**Fig. 5.** Optimized structure of reaction intermediates

Six electron/proton pairs alternately attacking the  $N_2$  molecule and first  $NH_3$  molecule is released in the fifth hydrogenation step. Figure 6 shows the free energy diagram for NRR on MoWC.  $N_2$  adsorption, which is the first step of NRR can occur spontaneously without the need of any additional energy. The first hydrogenation which results in the formation of  $*NNH$  species needs to overcome a barrier of 0.23 eV. In most of the NRR catalysts the first protonation step is typically the rate determining step. Since the molecule is elongated by  $0.22\text{\AA}$  in the case of MoWC, the activation is more and the barrier is relatively less. The second hydrogenation is exothermic with the release of 0.1 eV. The fourth hydrogenation step, which is the rate determining step (RDS) involves a free energy change of 0.52 eV. Although the sixth hydrogenation involves a higher free energy change (0.75 eV), the large amount of energy released during the preceding exothermic step compensates for it and can't be considered as the RDS. Hence the limiting potential of NRR for MoWC is governed by the fourth hydrogenation step which is -0.52 eV. Compared to pristine  $Mo_2C$ , which exhibits a limiting potential of -0.86 eV [29], the significantly reduced limiting potential of the Janus MoWC catalyst indicates enhanced favorability for NRR.

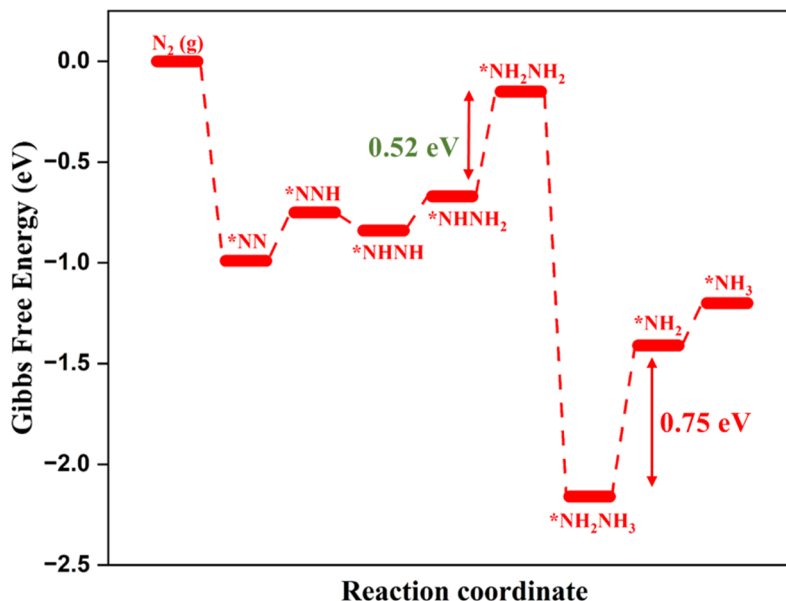


Fig. 6. Free energy diagram of NRR

HER is the main competitive reaction for NRR. The  $H^+$  ions can show an affinity for the same active sites on the surface of electro catalysts, which can lead to the  $H_2$  evolution at similar limiting potentials as NRR, which reduces the selectivity. In order to estimate the selectivity, H adsorption study is carried out on the catalyst. The adsorption energy of H atom ( $-0.71$  eV) is more positive than that of  $N_2$  ( $-1.51$  eV) demonstrating that the active sites interact more favorably with  $N_2$ . To further evaluate HER activity, the Gibbs free energy for H adsorption ( $\Delta G_H$ ) on the catalyst surface is calculated to be  $-0.47$  eV, which is significantly more negative than the ideal value ( $\Delta G_H=0$ ) indicating poor HER activity. Thus, the Janus MoWC catalyst exhibits excellent catalytic activity for NRR, along with favorable selectivity.

### 3.4 Comparison with other MXenes

To have more comprehensive idea, we made a comparison of  $\Delta G$  values of Janus MoWC with other well-known MXenes, as shown in Figure7. Our results reveal that Janus MoWC exhibits the lowest  $\Delta G$  among all the MXenes, highlighting its strong potential as a promising NRR catalyst.

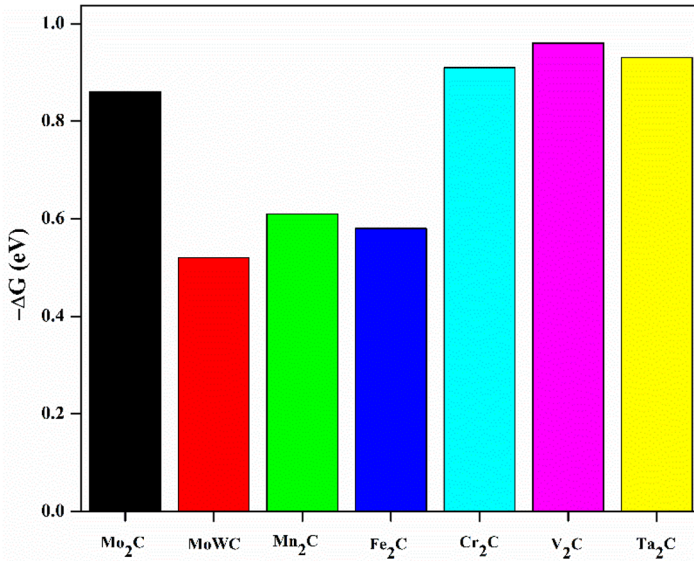


Fig. 7. Comparison of  $\Delta G$  values of other MXenes.

## 4 Conclusion

In this study we explored the catalytic activity of Janus MoWC derived from the pristine 2D Mo<sub>2</sub>C MXene. The electronic properties of the material are modified by surface engineering and hence the catalytic activity is enhanced. The Janus configuration improves N<sub>2</sub> adsorption and facilitates N≡N bond activation, favoring an enzymatic NRR pathway with a low energy barrier of 0.52 eV for the rate-limiting step. These results highlight Janus MoWC as a promising candidate for efficient and sustainable ammonia production.

**Acknowledgments.** The authors acknowledge the Center for Computational Modeling and Simulation (CCMS), NIT Calicut, for computational support and DST-SERB, Govt. of India, for project grant CRG/2021/002468.

**Disclosure of Interests:** The authors have no competing interests to declare that are relevant to the content of this article.

## References

- [1] V. Smil, 'Detonator of the population explosion', *Nature*, vol. 400, no. 6743, p. 415,

- 1999, doi: 10.1038/22672.
- [2] J. W. Erisman, M. A. Sutton, J. Galloway, Z. Klimont, and W. Winiwarter, 'How a century of ammonia synthesis changed the world', *Nat. Geosci.*, vol. 1, no. 10, pp. 636–639, 2008, doi: 10.1038/ngeo325.
- [3] J. Emsley, 'Going one better than nature?', *Nature*, vol. 410, no. 6829, pp. 633–634, 2001, doi: 10.1038/35070632.
- [4] Y. He *et al.*, 'Advancing the Electrochemistry of Gas-Involved Reactions through Theoretical Calculations and Simulations from Microscopic to Macroscopic', *Adv. Funct. Mater.*, vol. 32, no. 48, p. 2208474, Nov. 2022, doi: <https://doi.org/10.1002/adfm.202208474>.
- [5] J. S. Anderson, J. Rittle, and J. C. Peters, 'Catalytic conversion of nitrogen to ammonia by an iron model complex', *Nature*, vol. 501, no. 7465, pp. 84–87, 2013, doi: 10.1038/nature12435.
- [6] R. R. Eady, 'Structure–Function Relationships of Alternative Nitrogenases', *Chem. Rev.*, vol. 96, no. 7, pp. 3013–3030, Jan. 1996, doi: 10.1021/cr950057h.
- [7] Y. Ren, C. Yu, X. Tan, H. Huang, Q. Wei, and J. Qiu, 'Strategies to suppress hydrogen evolution for highly selective electrocatalytic nitrogen reduction: challenges and perspectives', *Energy Environ. Sci.*, vol. 14, no. 3, pp. 1176–1193, 2021, doi: 10.1039/D0EE03596C.
- [8] Y. Gao *et al.*, 'A theoretical study of electrocatalytic ammonia synthesis on single metal atom/MXene', *Chinese J. Catal.*, vol. 40, no. 2, pp. 152–159, 2019, doi: [https://doi.org/10.1016/S1872-2067\(18\)63197-3](https://doi.org/10.1016/S1872-2067(18)63197-3).
- [9] Y. Xia *et al.*, 'Thickness-independent capacitance of vertically aligned liquid-crystalline MXenes', *Nature*, vol. 557, no. 7705, pp. 409–412, 2018, doi: 10.1038/s41586-018-0109-z.
- [10] Q. Meng *et al.*, 'Theoretical investigation of zirconium carbide MXenes as prospective high capacity anode materials for Na-ion batteries', *J. Mater. Chem. A*, vol. 6, no. 28, pp. 13652–13660, 2018, doi: 10.1039/C8TA04417A.
- [11] X. Li, C. Wang, Y. Cao, and G. Wang, 'Functional MXene Materials: Progress of Their Applications', *Chem. – An Asian J.*, vol. 13, no. 19, pp. 2742–2757, Oct. 2018, doi:

<https://doi.org/10.1002/asia.201800543>.

- [12] J. Sun *et al.*, ‘Recent advances of MXene as promising catalysts for electrochemical nitrogen reduction reaction’, *Chinese Chem. Lett.*, vol. 31, no. 4, pp. 953–960, 2020, doi: <https://doi.org/10.1016/j.ccllet.2020.01.035>.
- [13] A. Y. Lu *et al.*, ‘Janus monolayers of transition metal dichalcogenides’, *Nat. Nanotechnol.*, vol. 12, no. 8, pp. 744–749, 2017, doi: [10.1038/nnano.2017.100](https://doi.org/10.1038/nnano.2017.100).
- [14] A. Rajan and R. Chatanathodi, ‘Computational Insights into the Catalytic Activity of Two-Dimensional Janus WSO for Hydrogen Evolution Reaction Computational Insights into the Catalytic Activity of Two- Dimensional Janus WSO for Hydrogen Evolution Reaction’, doi: [10.1149/1945-7111/adba15](https://doi.org/10.1149/1945-7111/adba15).
- [15] D. Er, H. Ye, N. C. Frey, H. Kumar, J. Lou, and V. B. Shenoy, ‘Prediction of Enhanced Catalytic Activity for Hydrogen Evolution Reaction in Janus Transition Metal Dichalcogenides’, *Nano Lett.*, vol. 18, no. 6, pp. 3943–3949, 2018, doi: [10.1021/acs.nanolett.8b01335](https://doi.org/10.1021/acs.nanolett.8b01335).
- [16] B. Akgenc, E. Vatansever, and F. Ersan, ‘Tuning of electronic structure, magnetic phase, and transition temperature in two-dimensional Cr-based Janus MXenes’, *Phys. Rev. Mater.*, vol. 5, no. 8, pp. 1–16, 2021, doi: [10.1103/PhysRevMaterials.5.083403](https://doi.org/10.1103/PhysRevMaterials.5.083403).
- [17] M. Das and S. Ghosh, ‘Improved Charge Storage Capacity of Supercapacitor Electrodes by Engineering Surfaces: The Case of Janus MXenes’, *J. Phys. Chem. C*, vol. 128, no. 3, pp. 1014–1023, 2024, doi: [10.1021/acs.jpcc.3c07443](https://doi.org/10.1021/acs.jpcc.3c07443).
- [18] S. Thasitha *et al.*, ‘First-principles study on structural stabilities, mechanical properties, and biaxial strain-induced superconductivity in Janus MoWC monolayer’, *Phys. Chem. Chem. Phys.*, vol. 26, no. 29, pp. 19696–19704, 2024, doi: [10.1039/d4cp01215a](https://doi.org/10.1039/d4cp01215a).
- [19] J. K. Nørskov *et al.*, ‘Trends in the Exchange Current for Hydrogen Evolution’, *J. Electrochem. Soc.*, vol. 152, no. 3, p. J23, Jan. 2005, doi: [10.1149/1.1856988](https://doi.org/10.1149/1.1856988).
- [20] G. Kresse and J. Hafner, ‘Ab initio molecular dynamics for liquid metals’, *Phys. Rev. B*, vol. 47, no. 1, pp. 558–561, 1993, doi: [10.1103/PhysRevB.47.558](https://doi.org/10.1103/PhysRevB.47.558).
- [21] G. Kresse and J. Furthmüller, ‘Efficiency of ab-initio total energy calculations for metals and semiconductors using a plane-wave basis set’, *Comput. Mater. Sci.*, vol. 6, no. 1, pp. 15–50, 1996, doi: [10.1016/0927-0256\(96\)00008-0](https://doi.org/10.1016/0927-0256(96)00008-0).

- [22] J. P. Perdew, K. Burke, and M. Ernzerhof, ‘Generalized Gradient Approximation Made Simple’, *Phys. Rev. Lett.*, vol. 77, no. 18, pp. 3865–3868, Oct. 1996, doi: 10.1103/PhysRevLett.77.3865.
- [23] P. E. Blöchl, ‘Projector augmented-wave method’, *Phys. Rev. B*, vol. 50, no. 24, pp. 17953–17979, Dec. 1994, doi: 10.1103/PhysRevB.50.17953.
- [24] S. GRIMME, ‘Semiempirical GGA-Type Density Functional Constructed with a Long-Range Dispersion Correction’, *Wiley InterSci.*, vol. 27, 2006, doi: 10.1002/jcc.
- [25] J. D. Pack and H. J. Monkhorst, ‘“special points for Brillouin-zone integrations”-a reply’, *Phys. Rev. B*, vol. 16, no. 4, pp. 1748–1749, 1977, doi: 10.1103/PhysRevB.16.1748.
- [26] J. K. Nørskov, T. Bligaard, J. Rossmeisl, and C. H. Christensen, ‘Towards the computational design of solid catalysts.’, *Nat. Chem.*, vol. 1, no. 1, pp. 37–46, Apr. 2009, doi: 10.1038/nchem.121.
- [27] Y. Khazaei, Mohammad and Arai, Masao and Sasaki, Taizo and Estili, Mehdi and Sakka, ‘Two-dimensional molybdenum carbides: potential thermoelectric materials of the MXene family’, *Phys. Chem. Chem. Phys.*, vol. 16, pp. 7841–7849, 2014.
- [28] R. F. W. Bader, ‘Principle of stationary action and the definition of a proper open system’, *Phys. Rev. B*, vol. 49, no. 19, pp. 13348–13356, 1994, doi: 10.1103/PhysRevB.49.13348.
- [29] K. Ba *et al.*, ‘Single Faceted Two-Dimensional Mo<sub>2</sub>C Electro-catalyst for Highly Efficient Nitrogen Fixation’, *ACS Catal.*, vol. 10, no. 14, pp. 7864–7870, Jul. 2020, doi: 10.1021/acscatal.0c01127.

**Open Access** This chapter is licensed under the terms of the Creative Commons Attribution-NonCommercial 4.0 International License (<http://creativecommons.org/licenses/by-nc/4.0/>), which permits any noncommercial use, sharing, adaptation, distribution and reproduction in any medium or format, as long as you give appropriate credit to the original author(s) and the source, provide a link to the Creative Commons license and indicate if changes were made.

The images or other third party material in this chapter are included in the chapter's Creative Commons license, unless indicated otherwise in a credit line to the material. If material is not included in the chapter's Creative Commons license and your intended use is not permitted by statutory regulation or exceeds the permitted use, you will need to obtain permission directly from the copyright holder.

